SPIDER

Spheroid's Panchromatic Investigation in Different Enviromental Regimes

December 9, 2008

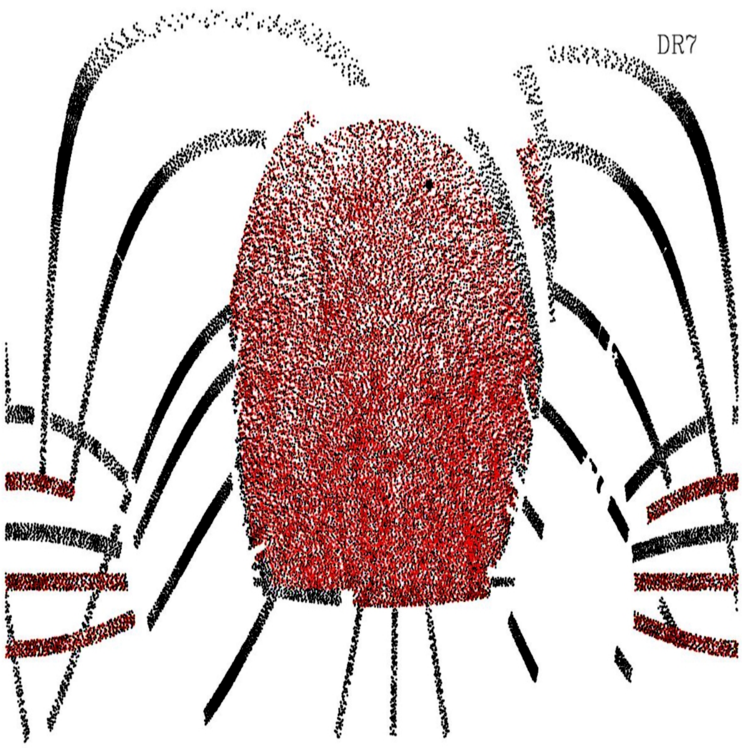

0.1 Background of the ETG project

Understanding the formation of massive stellar systems represents a continuing problem for modern cosmology. In broad terms, it is difficult reconcile the observed variation of galaxy properties with mass and the well-established model of hierarchical mass assembly. The concordant picture is that dark matter halos assemble through the continuous aggregation of lower mass units. Galaxies merge, building up their mass, and undergo morphological and spectrophotometric transformations.

In this framework, the study of early-type galaxies (ETGs) that represent the high end of the galaxy mass function in the local universe is of paramount importance. One naive expectation would be that more massive galaxies, which assembled at later times, should also have more recent and protracted star formation than low mass systems. However, a wealth of observational results has clearly shown that low mass galaxies ($M \lesssim 10^{11}\, M_{\odot}$) are actually younger than more massive ones. This is also known as downsizing in galaxy formation (Cowie et al. 1996). Current models of galaxy formation reconcile the downsizing scenario with the hierarchical model by introducing an *ad-hoc* mass dependent feedback mechanism, able to quench star-formation more efficiently in more massive galaxies, leading to the population of red, *passively evolving* spheroids we observe today. The main candidate for turning off star formation in massive systems is AGN feedback (Granato et al. 2001) that can either prevent gas cooling from the hot gas component in the halo (*radio mode*; e.g. Croton et al. 2006) or drive gas out of the central galaxy ('quasar mode' feedback; e.g. Hopkins et al. 2006). These mechanisms are believed to be related to the accretion of black holes in the center of galaxies, as mass assembly proceeds through mergers, and the triggering of central starbursts in galaxies resulting from merging of gas-rich systems.

There is a further manifestation of down-sizing which so far has not been extensively investigated. Properties of ETGs are expected to vary not only with stellar mass but also with the mass of the halo where the galaxy reside. Fig. 1 shows how the star-formation rates of model ellipticals are predicted to change as a function of the parent halo mass (from de Lucia et al. 2006, MNRAS). Rich clusters are expected to host ETGs with older ages and less protracted star formation than those in groups. This is further shown in Fig. 2, where we see that model ellipticals in rich clusters ($M_{200}(halo) > 10.^{14} M_{\odot}$) are expected to be $\sim$ 2Gyrs older and about 20% less metal-rich than those in the *field*. Similarly, semi-analytic models also predict a variation of ETG properties as a function of cluster-centric distance, in the sense that galaxies in cluster outskirts should be younger and less metal-rich than those in cluster cores. More massive galaxies form in the highest density peaks of the

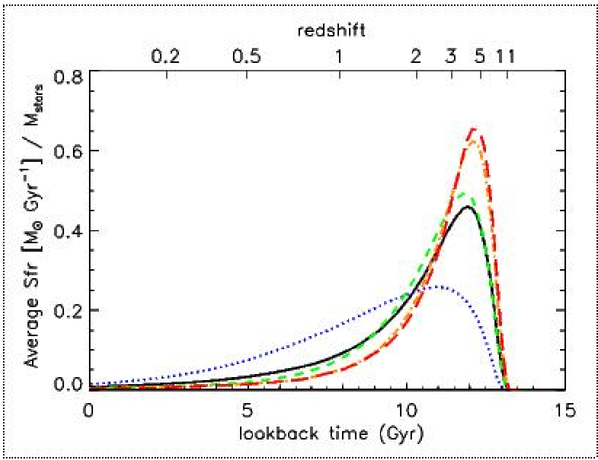

Figure 1: Star formation rate of model ellipticals residing in halos with virial mass $M_{200} \simeq 10^{15}$ (red), 10^{14} (orange), 10^{13} (green), and $10^{12} M_{odot}$ (blue) (from de Lucia et al. 2006). The solid curve shows the average star formation rate.

large scale structure (Mo & White, 1996) and thus have more time to merge within the halos (at cosmic epochs where the cluster velocity dispersion was low enough) and to interact with the intracluster medium. As galaxies infall into the cluster potential well, their star formation is expected to be turned off. Several mechanisms might contribute to this quenching, such as ram pressure stripping from the hot, intracluster medium (Gunn & Gott, 1972), galaxy harassment (Moore et al., 1999), tidal interactions (Bekki et al., 2001), and strangulation (Balogh et al., 2001). As mentioned before, galaxy merging within the halos is also the key ingredient for AGN feedback. Dissipationless interactions also appear to be important ingredients for the formation of ETGs, and can likely introduce a dependence of galaxy properties on the properties (e.g. the mass) of the halo where the galaxies reside. Dissipationless (dry) merging mixes stellar populations in galaxies, leading to somewhat flatter stellar population gradients (White, 1980). Moreover, it seems to be an essential ingredient in the origin of ETG scaling laws (e.g. Dantas et al. 2003). Several studies have suggested that dry mergers can be responsible for the mass assembly of ETGs to their final size (e.g. Bell et al. 2004; Faber et al. 2007) although there is no firm evidence for a decrease in the fraction of massive ETGs at high redshift (e.g. Cimatti et al. 2006). Semi-analytic models actually predict an increase in the number of stellar progenitors in more massive halos, with ETGs as massive as $10^{12} M_{\odot}$ experiencing several (dry) mergers events (up to five; see de Lucia et al. 2006).

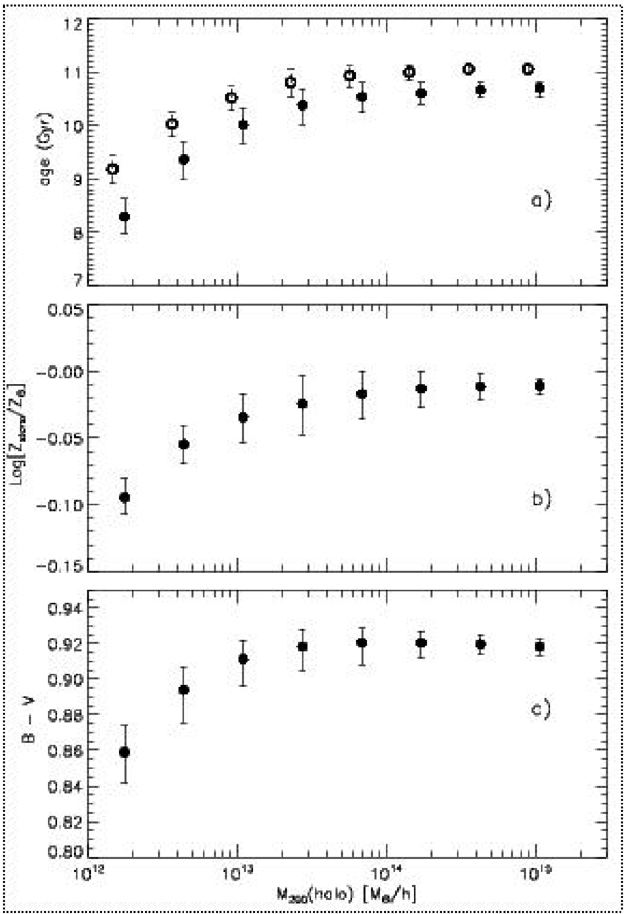

Figure 2: Age, metallicity, and color of model ellipticals as a function of the virial halo mass (from de Lucia et al. 2006).

Several studies agree on the fact that ETGs in the field are younger than those in high-density regions (see e.g. Bernardi et al. 2006). However, (Rogers et al., 2007) also found that ETGs in low density regions are less likely to show recent episodes of recent star formation, while a significant number of galaxies in high-density regions show signs of small but detectable recent star formation episodes. Both studies split the ETGs in two main branches, those in high and low density environments, with the high density bin including a wide range of local densities, from the center to the periphery of groups and clusters of galaxies. This can significantly wash out the environmental differences shown in Fig. 2.

So far, there is no detailed study analyzing the variation of ETG properties as a function of galaxy mass, parent halo mass, and clustercentric distance. This is the main goal of the ETG project. We want to study how properties of massive galaxies depend on galaxy mass, on radius, and mass of the cluster/group where galaxies reside, and how these dependencies relate to other global cluster properties (e.g. fraction of hot gas in the cluster, temperature, degree of substructures, etc). As shown from Figs. 2 and 1, the basic idea is that of comparing this environmental trend with model predictions, to better constrain the formation scenario of massive ellipticals.

One main problem in studying how the ETG properties respond to the halo mass is the continuing absence of a comprehensible and extended cluster catalog for the nearby Universe (z<0.1). The Abell cluster catalog is notoriously incomplete and heterogeneous as it comes from a visual inspection of plates. NoSOCS (Gal et al. 2008), while covering the largest area on the sky is based on poor quality plate data. With the advent of SDSS multiple new cluster catalogs have been generated: 1) C4 by Miller et al. (2005) is limited in area (DR3); 2) MaxBCG by Koester et al. (2007),is limited to higher redshifts (z>0.1); and 3) Berlind et al. (2006) is also limited in area (DR4). Since this project relies on DR6, defining a homogeneous and complete sample of clusters at z<0.1 is imperative. We are applying the Voronoi-Tessellation method to the DR7 spectroscopic catalog in order to create such a vital catalog. Furthermore, reliably defining to which cluster (or group) a given ETG is physically associated is also part of this project, for which we plan on using the caustic technique developed by Diaferio (1999). The distribution of galaxies in DR7 (photometric catalog) is shown in the front page of this document.

The project involves

1) constructing a large, complete sample of ETGs, well characterized by several observational properties such as luminosity, colors, velocity dispersions, structural parameters, internal color gradients, stellar masses, stellar population parameters (age, metallicity, enhancement), AGN signatures;

2) matching the ETG catalog to an objective, well-defined cluster catalog, well characterized in terms of several global cluster properties, such as cluster mass, virial radius, gas fraction, X-ray luminosity; and presence of substructures;

In the next section, we provide some details about the selection of the ETG sample, and the work done so far to derive galaxy photometric parameters.

0.2 The ETG sample

The ETG sample is selected from SDSS-DR6 (see La Barbera et al. 2008b). First, we select all galaxies in the redshift range of 0.05 to 0.095, with r-band Petrosian magnitudes [1] $\mathrm{M}_r < -20$. The lower redshift limit of $z = 0.05$ is chosen to minimize the aperture bias (Gómez et al., 2003), while the upper redshift limit guarantees a high level of completeness (see Sorrentino et al. 2006). The limit of $\mathrm{M}_r < -20$ roughly corresponds to the magnitude to which the SDSS spectroscopy is complete ($r \sim 17.8$), making the above sample approximately volume limited. Following Bernardi et al. (2003), we define as ETGs those objects with SDSS parameters $eclass < 0$ and $fracDev_r > 0.8$, selecting only those galaxies with available central velocity dispersion σ_0 between 70 and 420 $\mathrm{km\,s^{-1}}$ from SDSS-DR6 and having no spectroscopic warning flags set ($zWarining = 0$). These requirements yield a sample of $40,356$ ETGs. All these galaxies have $griz$ photometry and spectroscopy from DR6. Due to the low signal-to-noise ratio, we do not use u-band data from SDSS.

The above sample is matched to the fourth data release of UKIDSS–Large Area Survey (LAS). UKIDSS–LAS provides near-infrared photometry in the $YJHK$ bands over a sky region significantly overlapping the SDSS (Lawrence et al., 2007). Fig. 3 shows the trasmision curve of the SDSS+UKIDSS filters, while Fig. 4 exhibits the whole distribution of the ETGs on the sky. UKIDSS data in the YHK bands have a pixel scale of $0.4''/pixel$, matching the resolution of SDSS. Data in Y bands have a better resolution of $0.2''/pixel$. The $YJHK$ bands have average depths of 20.2, 19.6, 18.8, and 18.2 mags, respectively (point source detections at $5''$ within a $2''$ aperture). The matching was done by considering only frames with the better quality flag ($ppErrBits < 16$) The number of matched sources is maximum in J band, with 7674 ETGs. The number of matches is 5742, 6824, and 6941 galaxies in Y, H, and K bands, respectively. Considering ETGs simultaneously matched with two UKIDSS bands, $H + K$ gives the maximum number of 6625 objects. The number of matches does not vary significantly when considering either three bands or all the four wavebands. 5118 ETGs have photometry available in all four UKIDSS filters. Out of 40356 ETGs, we finally selected all the objects with available photometry in J-band, in $H + K$, and in $YJHK$.

Hence, the final sample of ETGs includes 40356 galaxies with available

[1] corrected for galactic extinction following Schlegel, Finkbeiner and Davis (1998) and k-corrected with $kcorrectv4\_1\_4$ (Blanton et al., 2003) through rest-frame filters blue-shifted by a factor $(1 + z_0)$. Following previous works (e.g. Hogg et al. 2004) we adopted $z_0 = 0.1$ which corresponds approximately to the upper redshift limit of the galaxy catalog.

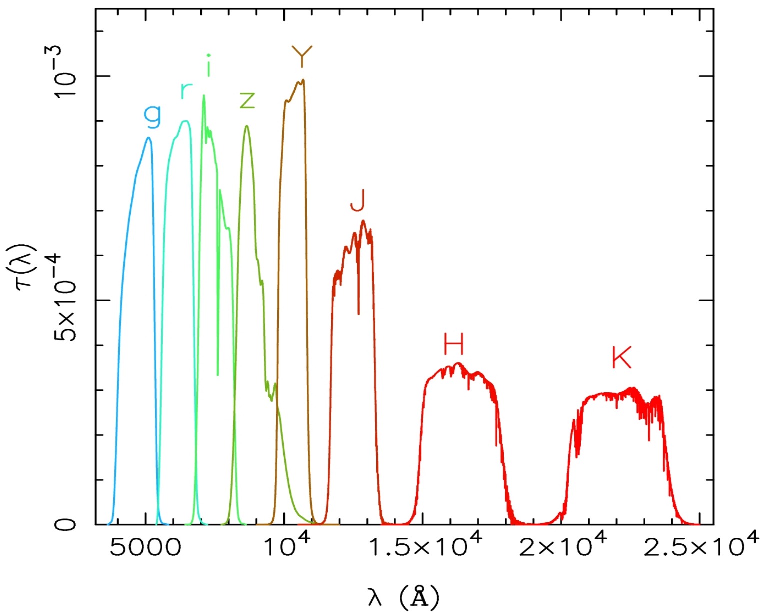

Figure 3: Trasmission curves for the $grizYJHK$ filters. Each curve has been normalized to an area of one.

photometry in $griz$ bands and spectroscopy from SDSS-DR6. Of these, about 6000 galaxies have NIR photometry in DR4 of UKIDSS-LAS.

0.3 Processing of the optical–NIR data

All of the optical griz images (31112 best reduced frames) for the ETG sample were retrieved from the SDSS archive and processed at the INPE-LAC cluster (Sao Jose dos Campos, Brazil) using 2DPHOT (La Barbera et al., 2008a) (hereafter LdC08). We ran 2DPHOT simultaneously on 40 CPUs, processing all the images in a given band in 1.5 days. The UKIDSS images were retrieved from the WFCAM Science Archive and processed at the Beowulf system available at INAF-OAC (Naples, Italy) A total of 12963 multiframes were retrieved and processed with 2DPHOT, running 32 CPUs simultaneously. The processing took half a day for each waveband. Both the optical and NIR images were processed in the same way.

2DPHOT is an automated software environment that performs several tasks, such as catalog extraction (using S-Extractor, Bertin & Arnout 1996), star/galaxy separation, and surface photometry. A complete description of the 2DPHOT package can be found in LdC08; here we provide a brief de-

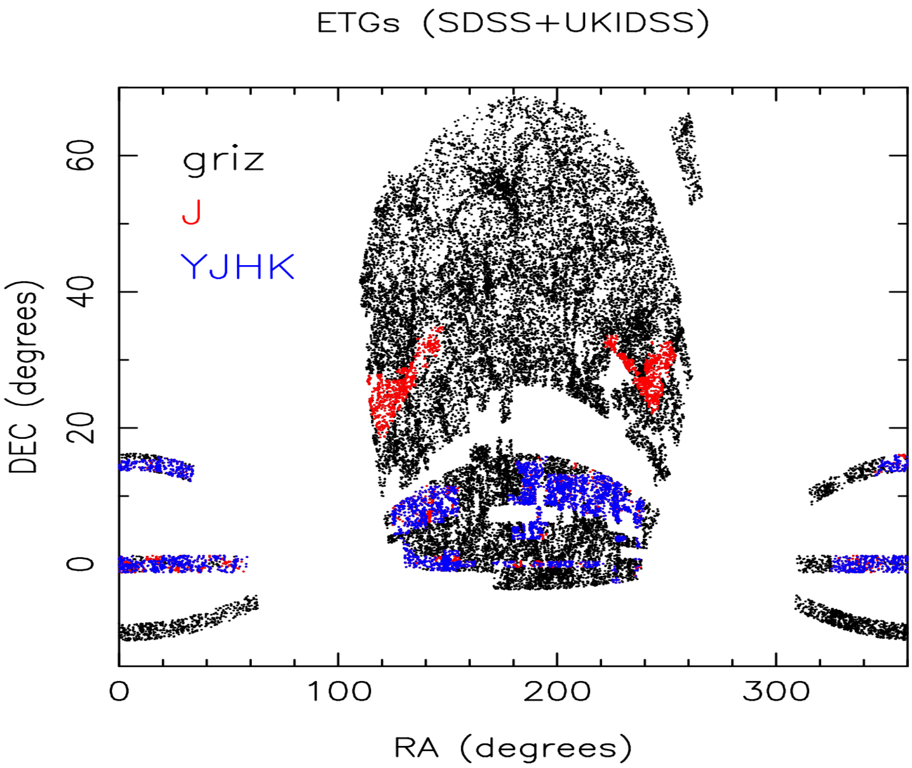

Figure 4: Distribution in RA and DEC of the ETG sample. Black points mark the optical $griz$ data, while red and blue symbols denote the J and YHK data, respectively. .

scription of the steps relevant for measuring the photometric parameters of the ETGs. For each galaxy, a local PSF model was constructed by fitting the four closest stars in the image with a sum of three two-dimensional Moffat functions. Isophotal distortions of star isophotes were modeled as described in LdC08. The parameters $r_{\rm e}$, $<\mu>_{\rm e}$ and n were then obtained by fitting galaxy images with PSF-convolved Sersic models. In the griz bands, we repeated the fitting twice. In a first step, where we obtain $r_{\rm e}$, $<\mu>_{\rm e,}$ and n, we fitted two-dimensional Sersic models having elliptical isophotes. The second fit was performed by using Sersic models whose isophotes deviate from the elliptical shape. The deviation is described by a fourth order cos term, whose coefficient (a_4) describes the boxiness ($a_4 < 0$) and diskyness ($a_4 > 0$) of the isophotal shape. We note that this method is somewhat different from the definition adopted by (Bender & Moellenhoff, 1987), where the peak value of a_4 is derived in a given radial range. The method above provides a global seeing de-convolved a_4 parameter. The second fitting was done only for the

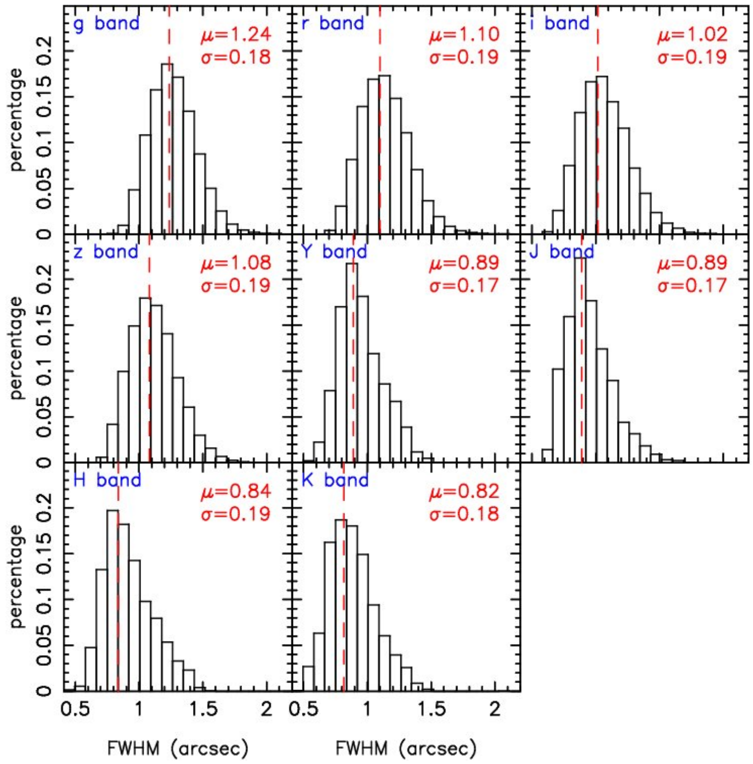

Figure 5: Distribution of seeing FWHM values for galaxies in $grizYJHK$ (from left to right and top to bottom). The median value, μ of each distribution is marked by the red dashed line in each panel. Both the value of μ and the standard deviation, σ. of the distributions are reported in the top-right corner of each plot.

$griz$ band images since they have a better signal-to-noise ratio.

Fig. 5 shows the distribution of seeing FWHM values for all galaxies in different bands. For each galaxy, the seeing FWHM is computed from the corresponding PSF model. As expected, the average FWHM value is larger in the blue than in the NIR. The peak value of the FWHM distributions varies from $1.24''$ in g-band to $0.82''$ in K-band, a relative variation of 34% (with respect to the g-band value). Moreover, in the $YJHK$ ($griz$) bands almost all galaxies have seeing FWHM better than $1.5''$ ($1.8''$), with 90% of the sample having seeing FWHM below $1.2''$ ($1.5''$).

Fig. 6 compares the distribution of χ^2 values from the two-dimensional fitting of galaxies in each band. The χ^2 is computed as follows. For each galaxy, we select only pixels 1σ above the local sky background. The selection is done from the two-dimensional seeing-convolved Sersic model. Then,

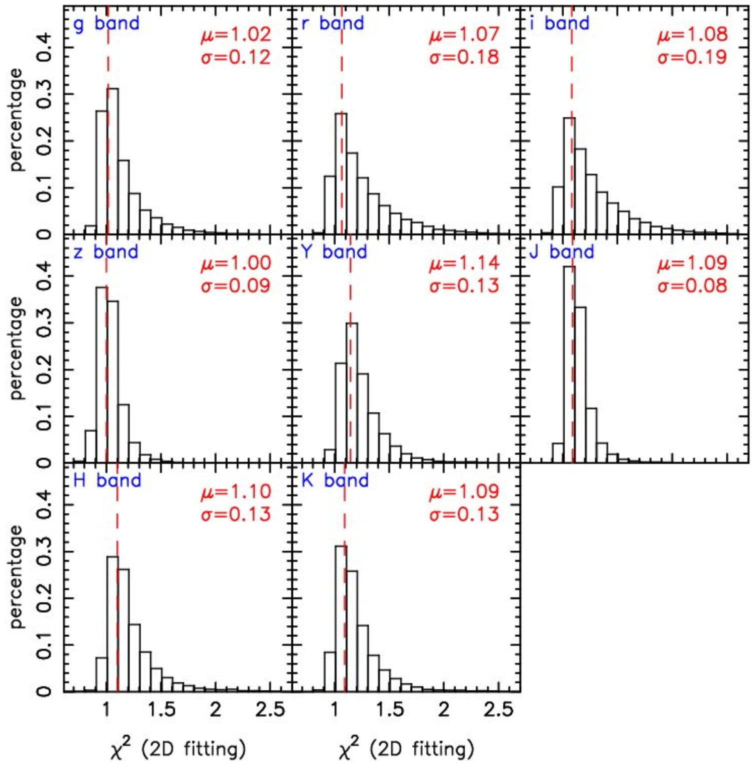

Figure 6: Same as Fig. 5 for the χ^2 of two-dimensional fitting in $grizYJHK$.

for the selected pixels, we compute the χ^2 as the rms of normalized residuals between the galaxy image and the model. Normalization is done by dividing the residuals by the expected noise in each pixel, accounting for both background noise and photon noise of the galaxy counts. The fact that all the peak values are slightly larger than one (except the z-band) is because (i) the 2D fitting minimizes the sum of squared residuals over the full galaxy stamp image, while here we are computing normalized residuals for pixels 1σ above the background; (ii) in a few pixels around the galaxy center larger residuals may be produced as a result of the discrete convolution of the two-dimensional Sersic model and the PSF. It is remarkable to see that all of the distributions are peaked around one, especially considering the σ values. Moreover, the NIR bands have a less pronounced tail of positive values than the optical bands. Positive values arise from faint morphological features (e.g. disk, spiral arms, etc...) in the sample of ETGs which are not accounted for by the two-dimensional model. This is shown in Fig. 7 and 8. Both figures show residual maps after model subtraction in the r-band. Fig. 7 displays

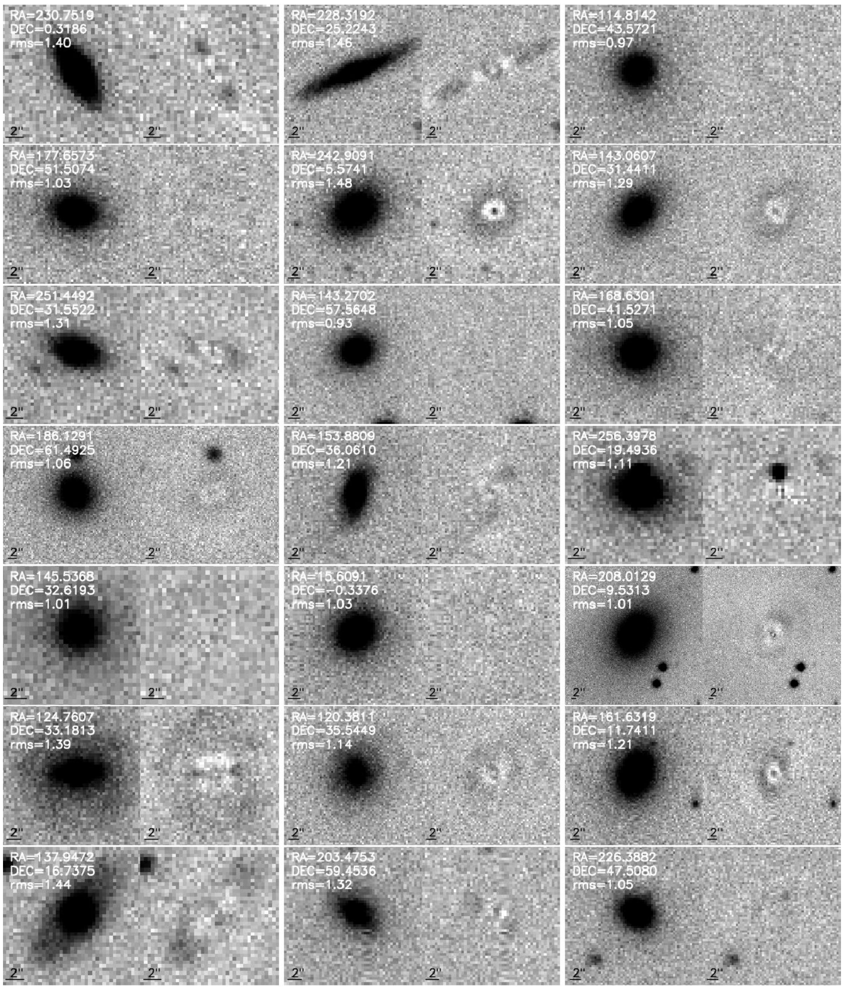

Figure 7: Two-dimensional fit results for galaxies in r-band with typical χ^2 value ($\chi^2 < 1.5$). Each plot shows the galaxy stamp (left) and the residual map (right) after model subtraction, using the same gray levels. The grayscale is proportional to the standard deviation of the background. The spatial scale is shown in the bottom-left corner of the left plots. For each galaxy image, the corresponding celestial coordinates and χ^2 value are reported in the upper-left corner.

cases where the χ^2 is very close to the peak value ($\chi^2 < 1.5$) while Fig. 8 plots cases with high χ^2 value ($1.5 < \chi^2 < 2.0$ in r-band). Usually, as the χ^2 value increases we see faint morphological feature appearing in the residual map. Most of these features are expected to disappear when moving to NIR bands.

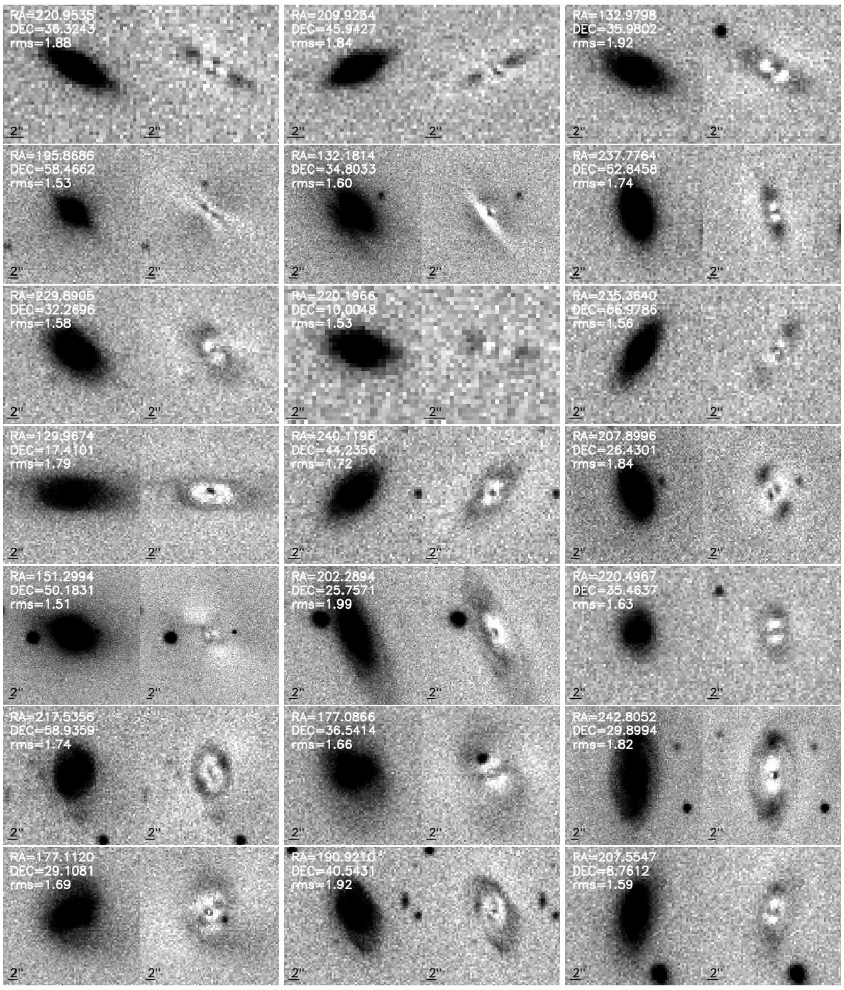

Figure 8: Same as Fig. 7 but for galaxies with high chi^2 value ($1.5 < \chi^2 < 2.0$ in r-band).

Fig. 9 compares the distribution of effective radii in the eight bands. The peak value of the distribution decreases smoothly from $0.53dex$ ($\sim 3.4''$) in g-band to $0.38dex$ in K ($\sim 2.4''$), corresponding to a relative variation of 40%. The decrease of effective radii is largely expected from the fact that ETGs have negative internal color gradients.

Fig. 10 compares the distributions of axis ratios, b/a, from the two-dimensional fitting in the eight bands. The median value (~ 0.69) and the shape of the distributions are identical for all the wavebands. As expected, the fraction of galaxies with low values of b/a decreases, with only a few percent of ETGs having axis ratios as low as 0.3.

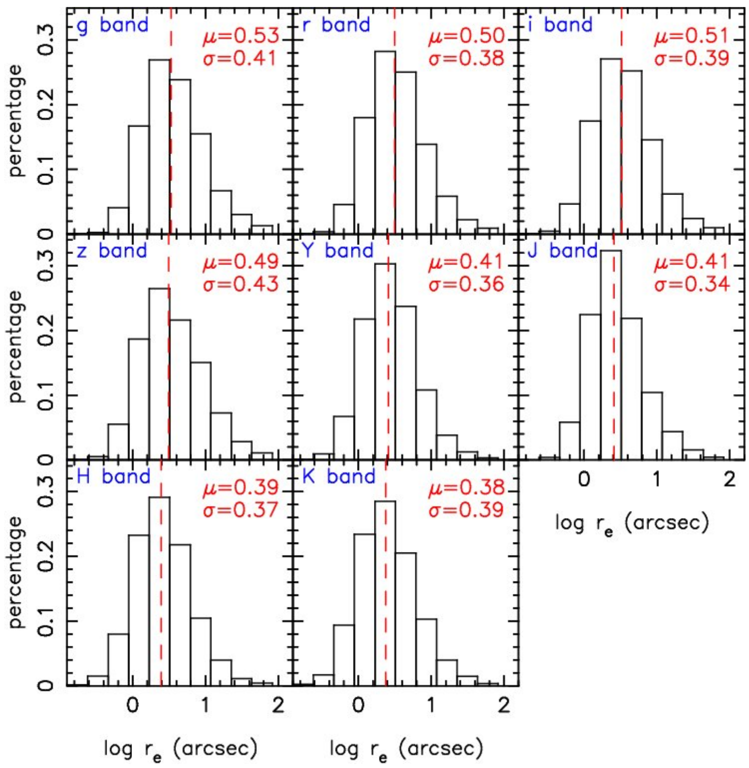

Figure 9: Same as Fig. 5 for the distribution of effective radii in each band.

Fig. 11 compares the distributions of the Sersic index, n. As expected from the selection of ETGs, almost all galaxies have Sersic index larger than 2.0, indicating that there are no disk-dominated systems in the sample. The distributions show a large scatter, with the values of n ranging from 2.0 up to $\sim$ 10. This value is still below the maximum value allowed (12) in the two-dimensional fitting algorithm. The median value of the distributions is around 6.0 for all the wavebands, although we see some variation in both the shape and the median value of the distributions. Particularly, the median value increases from $\sim$ 5.4 in g-band to 6.4 in z-band. It then decreases from z-band to J-band ($n \sim 5.5$) and again increases up to ~ 6.7 in K-band. Looking at the shape of the distributions, we see that they are peaked around $n \sim 4$ in gri, and then they become essentially flat in all the NIR waveband, from z to K, with the only exception of the J band where there is still a peak around $n \sim 4$. We note that observations and data reduction in J-band were carried out in a somewhat different way with respect to the other UKIDSS wavebands (see e.g. Warren et al.2007). Here, a micro-stepping procedure, with integer pixel offsets between dithered exposures is used. Images are

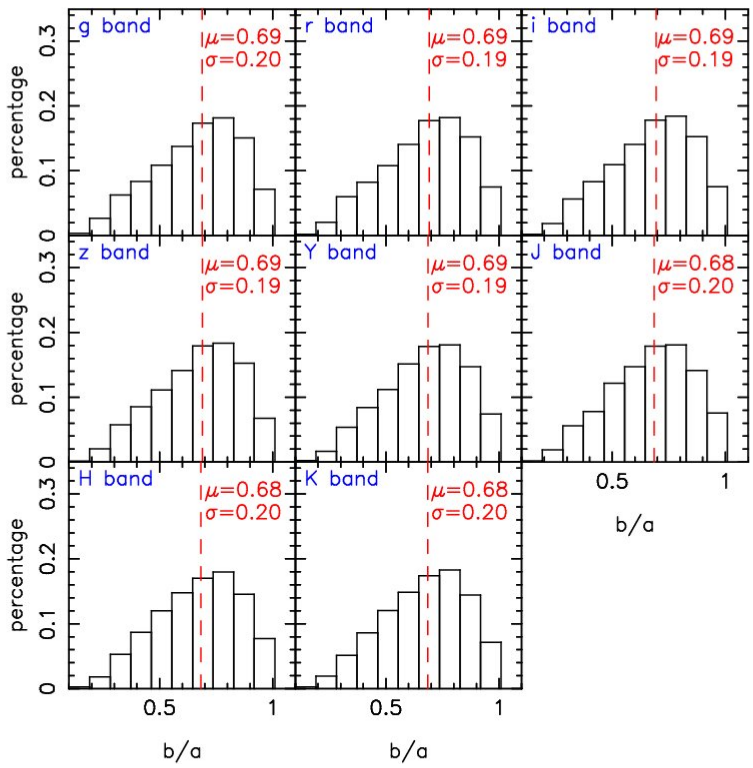

Figure 10: Same as Fig. 5 for the distribution of axis ratios.

interleaved to a subpixel grid and then stacked. This procedure results in a better image resolution of $0.2''/pixel$, with a better astrometric accuracy (useful for proper motions measurements). To see whether the difference in the J-band distribution of Sersic indices is statistically significant or an artifact of the different image processing, we repeated the two-dimensional fitting of galaxies in the J-band, by fixing the J-band Sersic index to the average value obtained with the H and K band images. Fig. 12 shows the relative variation of the best-fitting χ^2 values obtained when letting n vary versus keeping it fixed in the fit. The median relative variation is slightly negative, and the distribution also shows a more pronounced tail towards negative values, as expected by the fact that having n as a free parameter produces a lower χ^2 value. However, we see that the median offset is only $\sim -0.03\%$, which is indistinguishable from zero. Moreover, almost all galaxies have a relative χ^2 variation less than a few percent. This suggests that it might be more meaningful to fix the Sersic index of each galaxy to its median value from all the wavebands and repeat the two-dimensional fit. This would reduce significantly the error on n for each object and provide more accurate

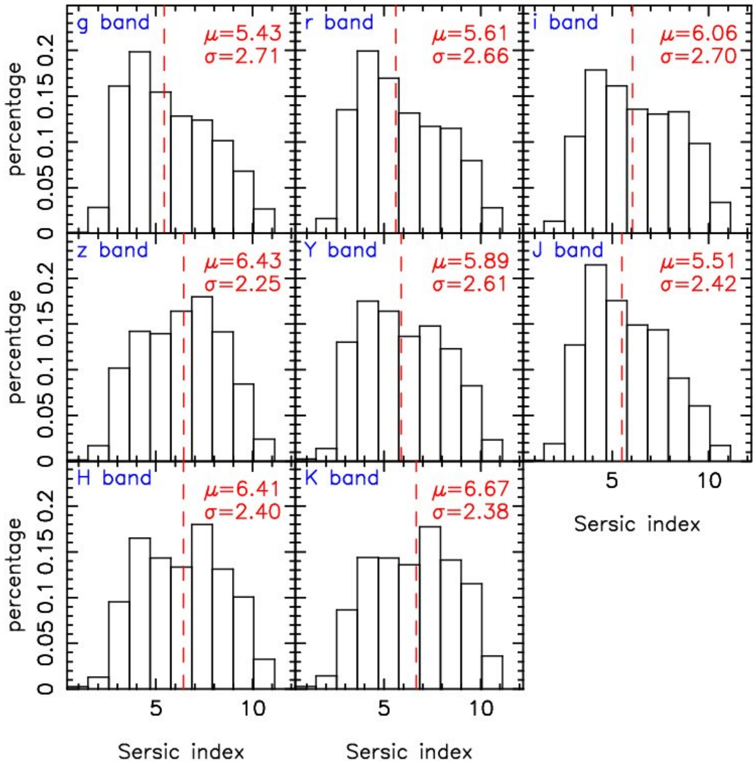

Figure 11: Same as Fig. 5 for the distribution of Sersic indices.

estimates of the structural parameters. A further test involving g and r bands, instead of J and $H + K$, will be done in the near future.

Finally, we report here some details about how we will measure magnitudes and colors for each galaxy in the sample.

All the magnitudes and $<\mu>_e$ values are corrected for galactic extinction and k-corrected. The distribution of galactic extinction for ETGs is shown in Fig. 13. Galactic extinction is estimated from the reddening maps of Schlegel, Finkbeiner, and Davis (1998), applying the correction of Bonifacio, Monai & Beers (2000) that reduces the $E(B - V)$ value in regions of high extinction ($E(B - V) > 0.1$). This correction is not included in the SDSS database. Fig. 13 shows that only a very small fraction of ETGs ($< 1\%$) has high reddening value ($E(B - V) > 0.1$).

We computed k-corrections using the $kcorrectv4\_1\_4$ software from (Blanton et al., 2003), which allows the correction to be done through restframe filters which are blue-shifted by a factor $(1 + z_0)$. For $z_0 = 0$, one recovers the usual k-correction. We have tested how the different waveband coverage can affect the k-corrections considering only the sample of 5118 galaxies

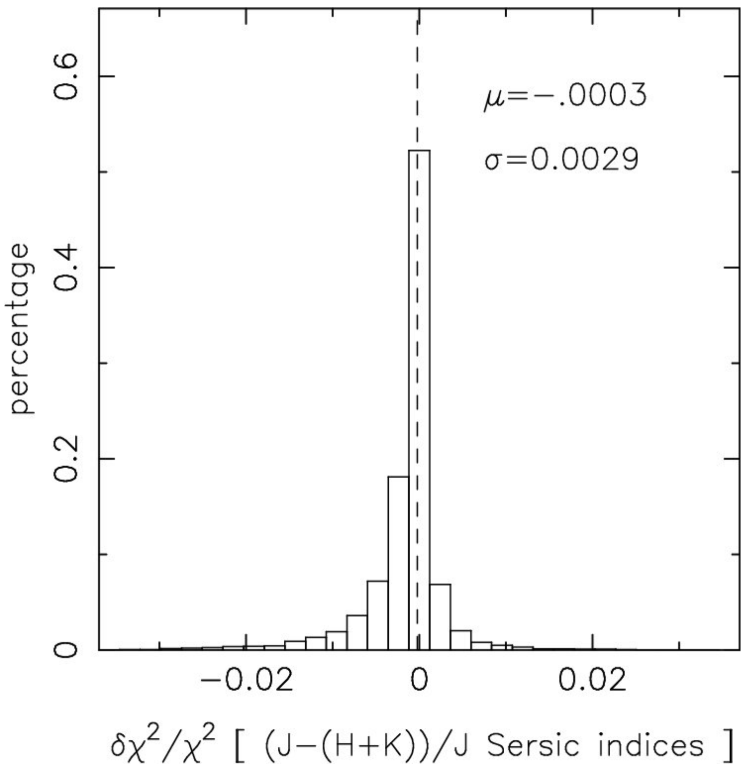

Figure 12: Relative variation of the χ^2 between the fits where n is a free parameter or is fixed to the H and K band values. The variation is computed with respect to the case with n as a free parameter. The dashed line mark the median value of the distribution, whose median, and standard deviation values, μ and σ, are reported in the upper–right corner.

with available information in all the $grizYJHK$ bands. For these objects, we have estimated k-corrections in $griz$ for two cases, where (i) we use all the eight wavebands and (ii) we use only the SDSS bands. Fig. 14 shows the variation of k-corrections with respect to the case where all the bands are used. To minimize seeing and aperture effects, for each galaxy and each band we used the MAG_AUTO magnitude in the S-Extractor catalog produced by 2DPHOT. The same figure also shows the case where total magnitudes from two-dimensional fitting are adopted. K-corrections are estimated by setting $z_0 = 0.0725$ which is the median redshift of the ETG sample. According to Blanton et al. (2003), this allows uncertainties on k-corrections to be minimized. The figure shows that k-corrections are very stable with respect to the adopted set of wavebands. The distributions are remarkably peaked around zero, with a standard deviation smaller than $0.01 mag$. Most of the galaxies have differences smaller than a few hundredths of a magnitude. The position of the peak is almost the same when using total magnitudes, though, as expected from the larger error of the total 2D fitting magnitudes, the width of the histograms is somewhat larger than for MAG_{AUTO} magnitudes. Fig. 15 shows the same comparison when considering the standard k-corrections, obtained by setting $z_0 = 0$. For each band, the peak of the distribution is sharply peaked around zero. However, in contrast to the case with $z_0 = 0.0725$, *standard* k-corrections are more dependent on the wavebands. A significant fraction of galaxies shows large k-correction differences, up to $0.2mag$

Fig.16 shows the LFs of ETGs in the $SDSS$ and $UKIDSS$ bands. Note that the LFs in all bands cover at least three magnitudes before the counts start dropping down, manifesting the incompleteness. Also, as we can see the completeness magnitude in r-band ($r \sim 17$) is brighter than the nominal value of 17.77 (Petrosian mags k-corrected with $z_0 = 0.1$) of SDSS spectroscopy. This might be explained by the difference in magnitude definition since we used Kron magnitudes here k-corrected to blue-shifted filters with $z_0 = 0.0725$.

0.4 Projects being done with these data

1 Establishing membership for the ETGs. To study how the ETG properties respond to the nearest bound structure we need first to establish membership. This will be done by applying the caustic technique (Diaferio 1999) and the virial analysis (Lopes et al. 2008).

2 α/Fe as a Star Formation Truncation clock. As suggested by de la Rosa et al (2007) it seems that the α/Fe parameter is related to the time where the last star formation event took place. Here, we may intuitively expect that in high density regions α/Fe should be larger, as it seems to be the result obtained by de la Rosa et al. (2007) examining a sample of ETGs in Compact Groups. The sample considered here in this project is the one needed to establish this link, so important for modeling galaxy evolution.

3 The ETG sample, thanks to the optical-NIR waveband coverage, can be used to disentangle between internal metallicity and age-gradients in ellipticals, and their dependence on global galaxy parameters (a_4, σ_0, stellar mass, stellar population parameters) and cluster properties (see La Barbera et al. 2005). It would be also interesting to see if any correlation exists among internal color gradients with (i) recent star

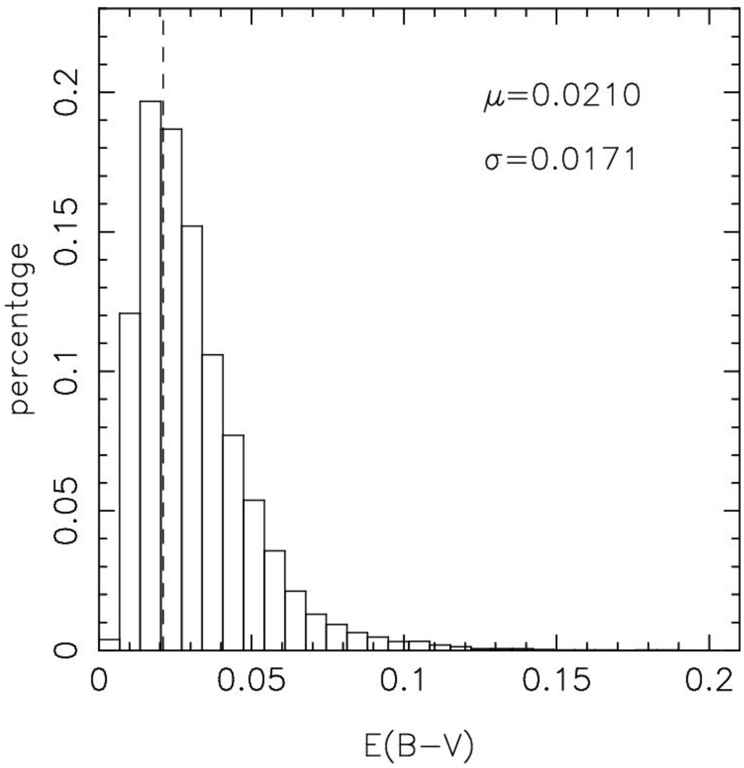

Figure 13: Distribution of galactic extinction values for ETGs. The peak value is marked by a dashed line. The peak value, μ, and the standard deviation, σ, of the distribution are reported in the upper–right corner.

formation in galaxies (from archive GALEX data), and (ii) amount of dust (other archive data ?).

4 Using the luminosity–size relation, one can look at differences of galaxy sizes at a given luminosity (stellar mass) as a function of the environment (clusters vs. groups and field, local vs. high density). If ETGs increase their size with redshift through dissipation-less encounters, one should detect size variations with environment.

5 The waveband dependence of the Fundamental Plane relation informs on how age and metallicity in ETGs change with their mass (see La Barbera et al. 2008b). These variations can be directly compared to model predictions (e.g. de Lucia et al. 2006), as a function of the environment where galaxies reside.

6 Using the large waveband baseline provided by the SDSS-UKIDSS data,

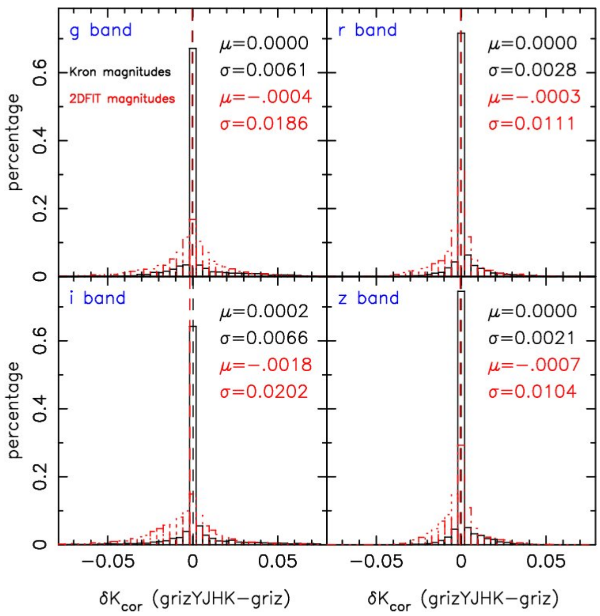

Figure 14: Differences of $z_0 = 0.0725$ k-corrections between the two cases where the $griz$ bands and all the eight wavebands are used.

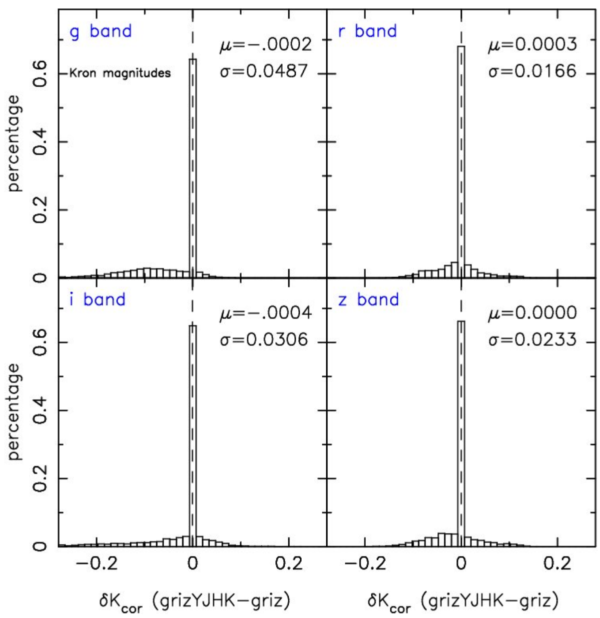

Figure 15: Same as Fig. 14 but for the standard $z_0 = 0$ k-corrections.

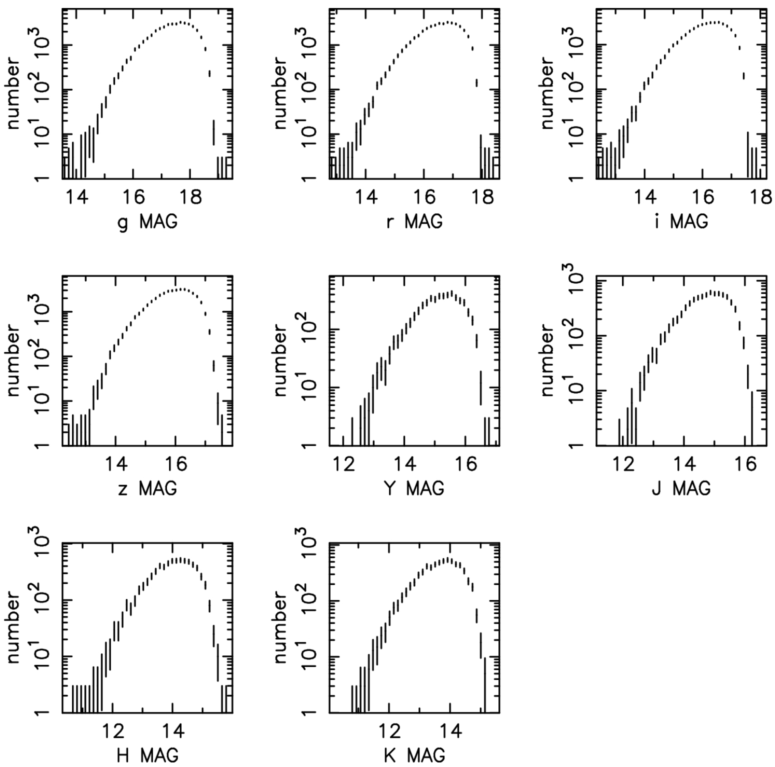

Figure 16: Luminosity functions of the ETG sample in $grizYJHK$ bands. We adopted Kron magnitudes, corrected for galactic extinction and k-corrected as explained in the text. Error bars are 2σ Poissonian uncertainties on number counts.

we can build-up color-magnitude relations and color-color digrams, and measure age vs. metallicity variations along the ETG mass sequence. We can test how (and if) these variations and the scatter around them depend on environment. Testing the assumption that the color-magnitude relation is a universal feature of ETGs is also of paramount importance for cluster finding algorithms themselves.

7 AGN feedback can affect the properties of the ICM. Measuring AGN signatures in ETGs and X-Ray properties of cluster/groups from RASS we can try to connect the these two aspects.

8 In the sample of ETGs, we see systems with faint morphological features (in the optical). Are scaling relations and environmental properties of these galaxies different from those of bona-fide ellipticals ?

Bibliography

Balogh, M.L., et al. 1999, ApJ, 527, 54

Bekki, M., Couch, W.J., & Shioya, Y. 2001, PASJ, 53, 395

Bell, E.F., et al. 2004, ApJ 608, 752

Bender, R., & Moellenhoff, C. 1987, A&A, 177, 71

Berlind, A.A. et al. 2006, ApJS, 167, 1

Bernardi, M., et al. 2003a, AJ, 125, 1849

Bernardi, M. et al. 2006, AJ 131, 288

Blanton, M.R., Lin, H., Lupton, R.H., et al., 2003, AJ, 125, 2276

Cimatti, A. et al. 2006, A&A, 453, 29

Cowie, Lennox L.; Songaila, Antoinette; Hu, Ester M.; Cohen, J. G. 1996, AJ 112, 839C

Croton, D.J. et al. 2006, MNRAS, 365, 11

Dantas, C.C. et al. 2003, MNRAS, 340, 398

de la Rosa, I.G., de Carvalho, R.R., Vazdekis, A., Barbuy, B. 2007, AJ, 133, 330

Diaferio, A. 1999, MNRAS, 309, 610

de Lucia, G., et al. 2006, MNRAS 366, 499

Faber, S.M., et al. 2007, ApJ 665, 265

Gal, R.R., e al. 2008, AJ, in press

Gunn, J.E., & Gott, J.R. 1972, ApJ 176,1

Gómez, P.L., et al. 2003, ApJ, 584, 210

Granato, G.L. et al. 2001, MNRAS, 324, 757

Hogg, D.W., Blanton, M.R., Brinchmann, J., Eisenstein, D.J., Schlegel, D.J., Gunn, J.E., McKay, T.A., Rix, H.W., Bahcall, N.A., Brinkmann, J., Meiksin, A. 2004, ApJ, 601, 29

Hopkins, P.F., et al. 2006, ApJS 163, 1

oester, B.P., et al. 2007, ApJ, 660, 239

La Barbera, F., de Carvalho, R.R., Gal, R.R., Busarello, G., Merluzzi, P., Capaccioli, M., Djorgovski, S.G. 2005, ApJ, 626, 19

La Barbera, F. et al. 2008, PASP, 120, 681

La Barbera, F: et al. 2008, ApJ, in press

Lawrence, A., et al. 2007, MNRAS, 379, 1599

Lopes, P.A., et al. 2008, MNRAS, in press

Miller, C.J., et al. 2005, AJ, 130, 968

Moore, B., et al. 1999, MNRAS, 304, 465

Mo, H.J., & White, S. 1996, MNRAS, 282, 347

Rogers, B. et al. 2007, MNRAS 382, 750

Schlegel, D., Finkbeiner, D.P., & Davis, M. 1998, ApJ, 500, 525 (SFD98)

Sorrentino, G., Antonuccio-Delogu, & V., Rifatto, A. 2006, A&A, 460, 673

White, S. 1980, MNRAS 191, 1